Potential for calcination of a palygorskite-bearing argillaceous carbonate

Victor Poussardin, Michael Paris, Arezki Tagnit-Hamou, Dimitri Deneele

Potential for calcination of a palygorskite-bearing argillaceous carbonate

Victor Poussardin[1,2], Michael Paris[1], Arezki Tagnit-Hamou[3], Dimitri Deneele[1,2*]

[1]*GERS-LGIE, Univ Gustave Eiffel, IFSTTAR, F-44344 Bouguenais, France*
[2]*Université de Nantes, CNRS, Institut des Matériaux Jean Rouxel, IMN, F-44000 Nantes, France*

[3]*Université de Sherbrooke, Sherbrooke, QC, Canada*

*corresponding author: dimitri.deneele@univ-eiffel.fr

Highlights

- The thermal reactivity of an argillaceous-carbonate sample is studied.
- A calcination temperature of 800°C allows a dehydroxylation of the clayey phases
- Evolution of the sample is quantified as a function of the calcination temperature
- The calcination leads to the formation of belite (C2S) from 700°C
- Calcined-Palygorskite-rich carbonate represents an opportunity for use as SCM

Abstract

The intensive use of cement as a building material causes significant pollution. The majority of CO_2 emissions come from the manufacturing process and not from the product itself. Indeed, the decarbonation of limestone and the use of fuels during clinkerisation are very polluting. One of the main solutions to reduce the environmental footprint of the cement industry is the use of Supplementary Cementitious Materials (SCMs) in substitution of clinker. Among them are glass powders, fly ashes, blast-furnace slags or calcined clays. This article focuses on the thermal reactivity of an argillaceous-carbonate sample containing palygorskite, smectite and dolomite. The sample was calcined at different temperatures and investigated using Solid State

Nuclear Magnetic Resonance (NMR), X-ray diffraction (XRD), and Scanning Electron Microscope (SEM). The increase in calcination temperature leads to an amorphisation of the clay fraction of the sample, resulting in a change in the coordination of the octahedral aluminium atoms. The progressive transformation of 6-fold aluminium atoms to 5-fold and 4-fold was quantified as a function of the calcination temperature. Furthermore, calcium issued from the decarbonation of dolomite reacts with silicon from the amorphisation of clay phases to form poorly-crystallized belite (C_2S). This dual system (pozzolanic and hydraulic) makes this sample a promising candidate as SCM in blended cements. The multi-technique analysis applied in this study allows to highlight a direct correlation between the calcination temperature and the induced structural modification.

Keywords: Palygorskite, calcination, belite, ^{29}Si NMR, ^{27}Al NMR, Rietveld refinement

1. INTRODUCTION

It is estimated that cement production is responsible for 5-8% of total anthropogenic CO_2 emissions (Huntzinger and Eatmon, 2009). In an international context promoting the reduction of CO_2 emissions, the cement industry appears to be a bad pupil. The fault resides in clinkerization, the process by which clinker, the basic product of Portland cement, is obtained. Both the use of mostly fossil fuels and the decarbonation of limestone during the process are contributing to the majority of CO_2 emissions (Cancio Díaz et al., 2017). Faced to this alarming observation, the cement industries are now turning to the research and development of new supplementary cementitious materials (SCMs) that can partially replace clinker in order to drastically reduce CO_2 release and the environmental cost of Ordinary Portland Cement (OPC) manufacture. These innovations include the use of additives from industry (blast furnace slags (Escalante et al., 2001), fly ash from power plants (Sakai et al., 2005)), natural additives (clays (Horpibulsuk et al., 2012)) and artificial additives (calcined clays). The Limestone Calcined

Clay Cement (LC^3) project (Scrivener et al., 2018) is a good example of the use of calcined clay as SCM. The substitution of 50% of the clinker with 20% limestone and 30% metakaolin reduces the environmental footprint of OPC by 20-23% while maintaining the delivery of cement with satisfactory mechanical properties (Cancio Díaz et al., 2017). Numerous studies have shown that kaolinite dehydroxylation during calcination leads to the production of very reactive SCM metakaolin, (El-Diadamony et al., 2018). In addition, the available kaolinite resources with potential for calcination are relatively well distributed on earth (Prasad et al., 1991), making it possible to envisage large-scale use. In this context, the majority of scientific research has been focused on the calcination of kaolins, sometimes neglecting the study of less common clays. However, understanding the reactivity of other types of natural materials containing clays is essential to envisage the valorisation of secondary clayey resources, refine our knowledge and propose new innovative solutions to reduce the CO_2 emissions of the OPC production. Natural samples rich in palygorskite are one of these interesting materials to test as SCM.

Palygorskite is a clayey mineral consisting of TOT-type ribbons. Several studies have shown that TOT clays, mainly montmorillonites and illites, are not ideal as SCM (Hollanders et al., 2016; Danner et al., 2018), mainly due to the resistance of their structure to heat treatment. The particularity of palygorskite structure compared to montmorillonite and illite is that the tetrahedra are reversed when passing from one ribbon to the other. This alternation creates channels that are filled with zeolitic water, and confers to palygorskite a three-dimensional structure (Galan, 1996). These channels provide to the palygorskite an important internal surface and hence large specific surface area, high sorption capacity, and microporosity. Its general formula is $(Mg,Al)_2Si_4O_{10}(OH).4H_2O$ but isomorphic substitutions are possible, in particular of silicon by aluminium in tetrahedral sheets (Blanco et al., 1989).

As specified above, the latest studies on blended cement deal with the addition of metakaolin and calcium carbonate to the blended cement. Indeed, limestone will improve the hydration reactions of the different phases of the clinker by acting as a nucleation surface for the hydrates produced. It will also react with the active alumina (from calcined clay) to form carboaluminates. These carboaluminates will stabilize the Ettringite that forms at the early stages of hydration and prevent its transformation into monosulphate. The Ettringite thus stabilised can fill more space than in the monosulphate form, helping to improve the mechanical properties (Bonavetti et al., 2001; Ipavec et al., 2011).

However, only few studies describe the addition of a calcined natural argillaceous-carbonate (Danner et al., 2018; Soltani et al., 2018). Then, we decided to progress by studying the potential for calcination of an argillaceous-carbonate containing palygorskite as a potential SCM. The aim is to describe the physico-chemistry of the raw material, to identify and understand the physicochemical modifications induced by the calcination, and to define its optimum calcination temperature.

2. MATERIALS AND EXPERIMENTAL METHODS

2.1. Material

The studied sample is a mining waste collected from a phosphate sedimentary deposit of a late Cretace-Eocene age. The series includes carbonates, marl, silex and clayey layers that are inserted between phosphate-rich layers, not exploited and considered as waste or a secondary resource to valorise. Sample was received in the form of loose blocks and was crushed and homogenized.

2.2. Calcination

The raw sample was calcined in alumina crucibles (about 3g of sample per crucible) using a laboratory furnace without atmosphere control. The furnace used was a silicon carbide

laboratory chamber with a maximum operating temperature of 1500°C. The sample was heated from 20°C up to 600, 700, 800 and 900°C with a heating rate of 300°C/h and a maximum temperature time of 1h. The cooling rate was not controlled (inertia of the furnace door closed) and the sample was collected after cooled down to room temperature (20°C). The choice of this calcination protocol was made in accordance with the existing bibliography (Garg and Skibsted, 2014, 2016; Danner et al., 2018; Krishnan et al., 2019; Trümer et al., 2019).

2.3. X-ray diffraction analysis

X-ray diffraction analysis were performed using a Bruker D5000 diffractometer with a Bragg-Brentano geometry. The source consists of a Cu anode tube (40 kV / 40 mA) that emits Cu Kα1 X-ray radiation (8 keV) of a wavelength λ = 1.5418 Å. The diffractograms of disoriented powders were recorded between 3° and 90° 2θ with a step size of 0.026° 2θ and a measurement time of 17s per step.

The diffractograms used for Rietveld quantification were acquired on a Bruker D8 diffractometer with a Bragg-Brentano geometry, using Cu anode tube, with Ni filter and without monochromator. The diffractograms were acquired between 4° and 90° 2θ with a step size of 0.018° 2θ and a measurement time of 6s per step. The quantification of the crystalline phases was made by Rietveld refinement using the open source Rietveld refinement program BGMN with Profex 4.0 interface (Doebelin and Kleeberg, 2015), the amorphous phase was quantified by using corundum (alpha-phase, 99.95% min) as an internal standard (see supporting informations).

2.4. Nuclear magnetic resonance

The ^{27}Al NMR MAS spectra were acquired using a 2.5 mm MAS probe on a Bruker Avance III 500 MHz spectrometer. A $\pi/13$ excitation pulse length was used for a radio frequency field of 11 kHz. The MAS frequency was 30 kHz. The repetition time was 1s.

The MAS ^{29}Si spectra were acquired using a 7 mm MAS probe on a Bruker NEO 300 MHz spectrometer. The rotor rotation speed was 5 kHz and the pulse length was $\pi/2$. Different repetition times between scans were tested to ensure quantitative results and the choice was made to use a time of 10s. It is important to note that the repetition time of 10s chosen is too short to obtain a quantitative signal from the Quartz. Indeed, due to its high crystallinity, a longer repetition time would be mandatory. However, in the present study, Quartz is unreactive and shorter repetition time can be used to save spectrometer time.

^{1}H decoupling was performed during the acquisition on all spectra. ^{27}Al and ^{29}Si spectra are reference against an aqueous solution of $Al(NO_3)_3$ and TMS (Tetramethylsilane), respectively. Finally, spectral decompositions were realized using the dmfit software (Massiot et al., 2002).

2.5. Scanning electron microscopy

The raw sample as well as changes induced by calcination were examined by scanning electron microscopy (SEM) using a Hitachi SU5000 microscope. The samples (raw fragment, raw powder, calcined powder) were subjected to a silver coating before observations.

3. CHARACTERIZATION OF THE RAW MATERIAL

A chemical analysis of the raw sample was carried out by X-Ray Fluorescence (XRF), the proportions of oxides (expressed in weight %) are presented in Table 1.

Table 1: Chemical analysis of the raw argillaceous-carbonate

Oxide	FeO	CaO	SiO_2	Al_2O_3	K_2O	TiO_2	Na_2O	V_2O_5	P_2O_5	MgO	LOI (1000°C)
wt.%	1.99	19.83	33.3	8.94	1.24	0.34	0.32	0.16	1.49	9.91	35.0

The oxides present in the highest quantity are SiO_2 (33.3 wt.%), CaO (19.83 wt.%), MgO (9.91 wt.%) and Al_2O_3 (8.94 wt.%). There is also a significant amount of FeO (1.99 wt.%), K_2O (1.24 wt.%) and P_2O_5 (1.49 wt.%).

Figure 1 displays the diffractograms of the raw argillaceous-carbonate samples. The characteristic peaks of palygorskite (W.F.Bradley, 1940) ([110] 2θ=8.43°, [200] 2θ=13.73°, [130] 2θ =16.26°, [040] 2θ=19.92) are observed. There is also a wide peak at around 2θ=6.2° which is characteristic of the [001] peak of Ca-Smectite (Bala et al., 2000). The width of this peak reflects the low crystallinity of this phase. palygorskite and Biotite, on the other hand, seem to be better crystallized because their peaks are much thinner. The other main crystalline phases composing this sample are dolomite, quartz, botite and hydroxylapatite. Table 2 presents the results of the Rietveld refinement of the raw material (details in Supporting Information).

The sample is mainly composed of dolomite (Dol = 53 wt.%) associated with palygorskite (Pal = 17.45 wt.%), Ca-smectite (Sm = 15.58 wt.%), quartz (Qz = 8.00 wt.%), hydroxylapatite (Hy = 3.00 wt.%) and biotite (Bio = 2.41 wt.%). The addition of corundum as an internal standard did not reveal the presence of amorphous phases. Therefore, Ca-smectite, palygorskite and biotite are the only sources of aluminium. Ca-smectite, palygorskite, biotite and quartz are the only sources of silicon in the material.

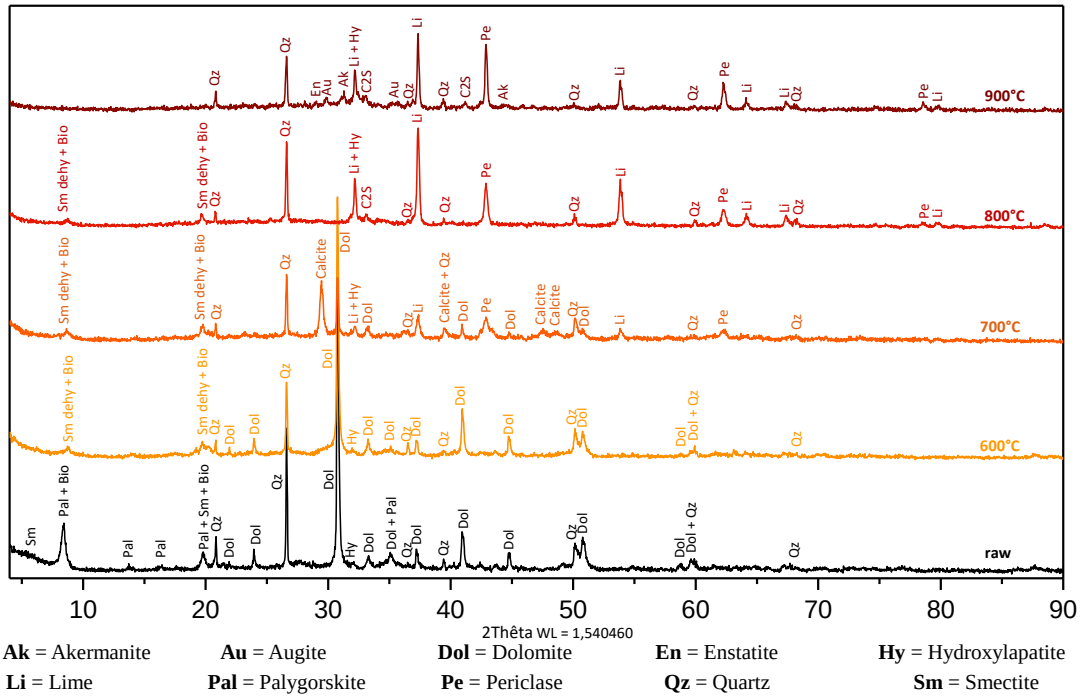

159

160 Figure 1 : Evolution of the X-ray diffractograms of the samples as a function of the

161 calcination temperature

162 Table 2: Wt.% of the crystalline phases of the raw and 800°C argillaceous-carbonate samples.

163 dolomite (Dol), biotite (Bio), lime (Li), periclase (Pe), palygorskite (Pal), Ca-smectite (Sm),

164 Ca-smectite dehydrated (Sm dehy), quartz (Qz), hydroxylapatite (Hy), hematite (He), belite

165 (C_2S), Am (Amorphous)

Raw	**Phase**	**Dol**			**Pal**	**Sm**	**Qz**	**Hy**	**Bio**		
	wt.%	53.58 (+/- 0.48)			17.45 (+/- 0.35)	15.58 (+/- 0.54)	8.00 (+/- 0.24)	3.00 (+/- 0.14)	2.41 (+/- 0.22)		
800°C	**Phase**	**Li**	**Pe**	**He**	**Pal**	**Sm dehy**	**Qz**	**Hy**	**Bio**	**C2S**	**Am**
	wt.%	19.41 (+/- 0.43)	17.11 (+/-0.37)	1.45 (+/- 0.10)	0.00	13.48 (+/- 0.48)	11.19 (+/- 0.27)	4.07 (+/- 0.17)	1.00 (+/- 0.19)	4.45 (+/- 0.20)	27.90 (+/- 1.60)

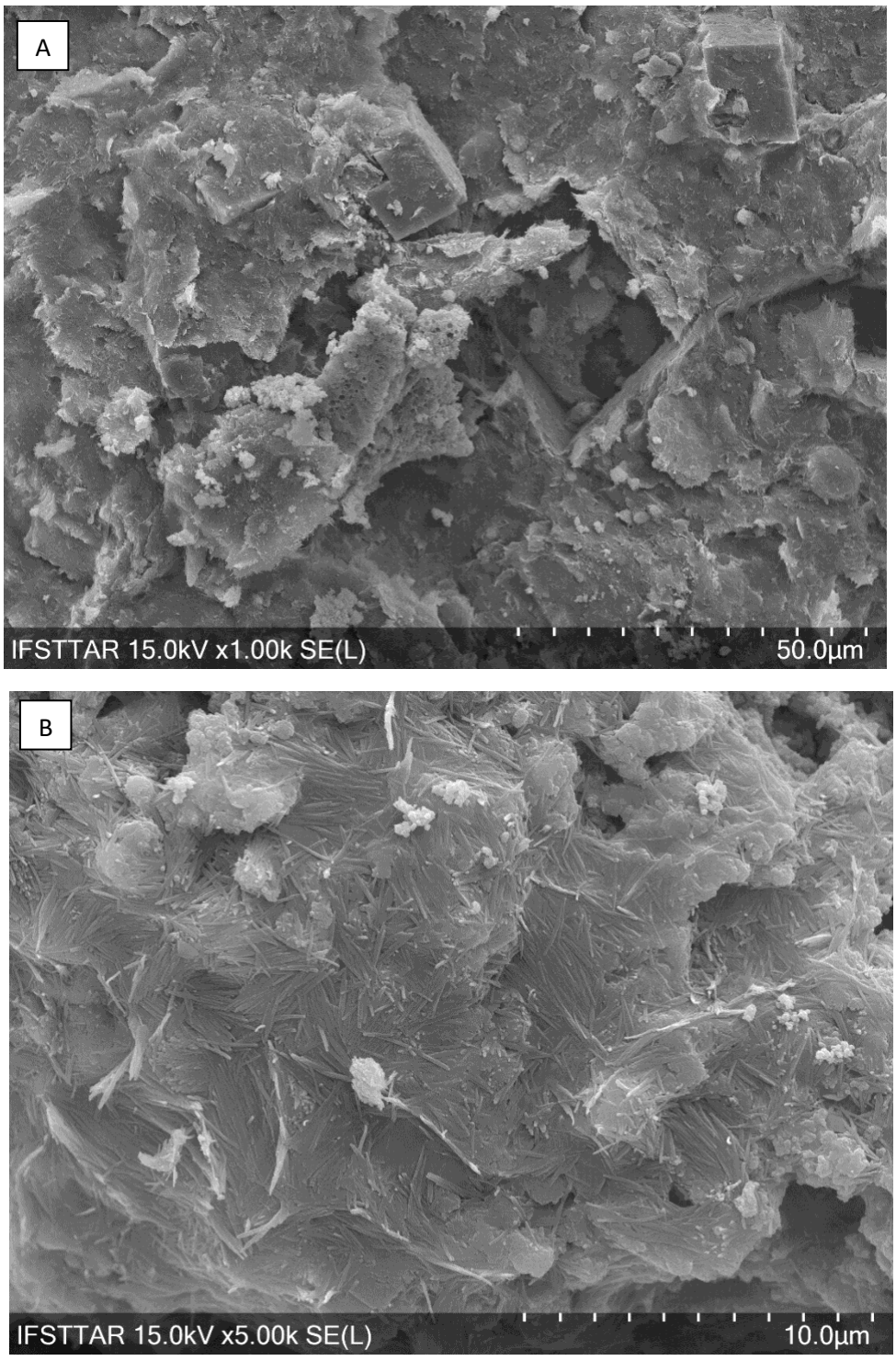

Figure 2: Scanning Electron Microscope images of the raw argillaceous-carbonate

Figure 2 displays two SEM images (A and B) of a fragment of the raw argillaceous-carbonate sample. Figure 2A shows the global morphology of the raw sample. dolomite rhombohedra are

clearly visible as well as the presence of a coating covering the entire sample. Figure 2B displays another image of the surface of the sample at a higher magnification. The layer covering the sample consists of a veil and very fine needles which are respectively characteristic of smectite and palygorskite (Boudriche et al., 2011). It therefore appears that palygorskite and smectite acts as a binder between the minerals in the sample and is present throughout the entire sample. This latter information completes the analysis made by XRD. Despite its average mass proportion (about 17 wt.%), the palygorskite is homogeneously distributed throughout the entire sample and is in contact with all phases.

The ^{27}Al MAS NMR spectrum of the raw argillaceous-carbonate sample is shown in Figure 3. It exhibits two main resonances at 3 and 70 ppm. The first intense resonance (3 ppm) corresponds to hexacoordinated aluminium (Maia et al., 2014) and can be associated with aluminium present in the palygorskite, Ca-smectite and biotite octahedra. The second resonance at 70 ppm corresponds to tetracoordinated aluminium (Maia et al., 2014) and can be associated with substitution of silicon atoms by aluminium atoms in the Ca-smectite and/or palygorskite tetrahedra (Sanz and Serratosa, 1984), and to a lesser extent to aluminium present within the biotite tetrahedral sheets. There is also the presence of weak resonance at approximately 57 ppm which can be associated with AlO_4 $q^4(4Si)$ (Muller et al., 1986). Aluminium present in the $q^4(4Si)$ configuration seems to be associated with a phase in very low quantity and/or composed of very small crystallites since the latter is not detectable by XRD.

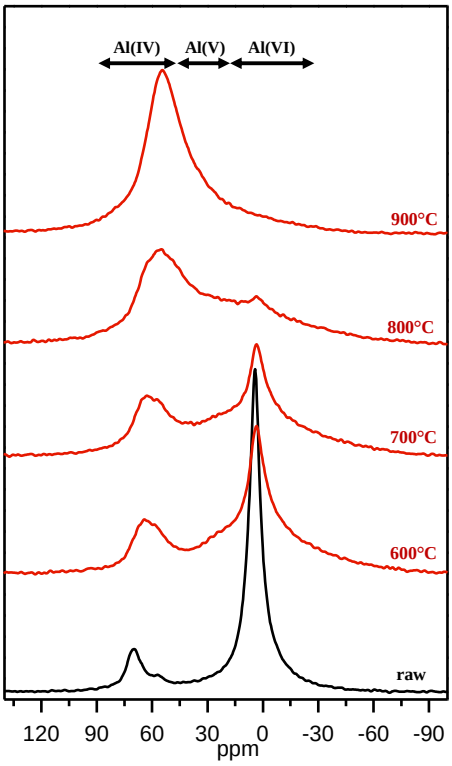

205

206 Figure 3: Evolution of the ^{27}Al MAS NMR spectra of the argillaceous-carbonate as function
207 of the calcination temperature.

208 Figure 4 displays the ^{29}Si MAS NMR spectrum of the raw sample. The two main resonances at
209 -92 and -98 ppm are attributed to palygorskite. They correspond to silicon in Q3 configuration
210 at the center and at the edges of the ribbons of tetrahedra, respectively (Barron et al., 1985).
211 The high intensity of resonances characteristic of palygorskite demonstrates its good
212 crystallinity. In addition, Ca-smectite and biotite revealed by XRD analysis also contribute to
213 the total ^{29}Si NMR signal. Indeed Q3 of Ca-smectite exhibit resonance at -93 ppm (Brown et
214 al., 1987) and Q2(1Al) of biotite resonates at -86 ppm (Mackenzie et al., 1987).

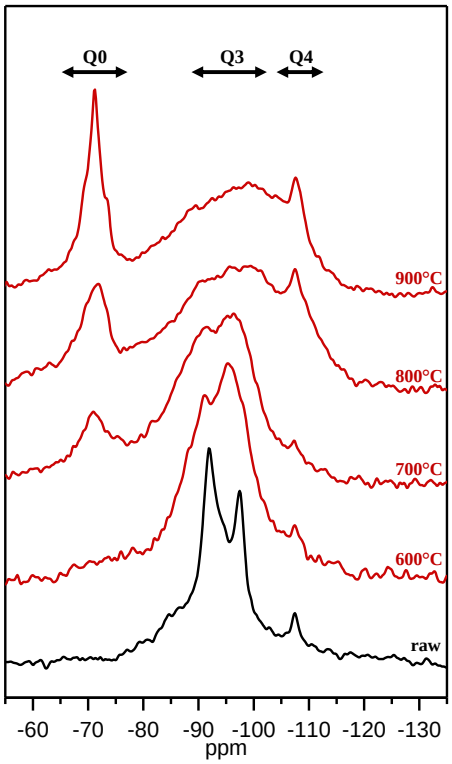

Figure 4: Evolution of the ^{29}Si MAS NMR spectra of the argillaceous-carbonate as a function of the calcination temperature.

The resonance observed at -108 ppm corresponds to the quartz in the sample (Lippmaa et al., 1980). The low resonance intensity at -93 ppm characteristic of smectite is explained by its very low crystallinity. Indeed, the existence of a local environment distribution for silicon atoms results in a broadening of the resonance, which is consistent with the observation made by XRD which suggests that Ca-smectite is very poorly crystallized.

4. EFFECTS OF CALCINATION

Figure 1 displays the evolution of the X-ray diffractograms of the samples as a function of the calcination temperature. Above 600°C, there is the disappearance of the peaks of palygorskite. This indicates a loss of crystallinity of the palygorskite phase in the sample. The shift of the

[001] characteristic peak of the Ca-smectite from about $2\theta = 6.2°$ to $2\theta = 8.75°$ is caused by the decrease of the d001 value due to the removal of the water from the interfoliate space. This observation is in accordance with previous works on the dehydration of Ca-smectite (Bala et al., 2000; Morodome and Kawamura, 2009). Above 700° the intensities of the characteristic peaks of dolomite decrease and new peaks attributed to calcite, periclase and lime, appear. These results agree with the existing bibliography (Olszak-Humienik and Jablonski, 2015) describing the thermal decomposition of dolomite as a two-stage process which proceeds as follows :

$$\mathbf{CaMg(CO_3)_2 \rightarrow CaCO_3 + MgO + CO_2}$$

$$\mathbf{CaCO_3 \rightarrow CaO + CO_2}$$

At 800°C all the characteristic peaks of dolomite and calcite have disappeared, demonstrating its full dissociation. On the other hand, we observe the appearance of a diffraction peak at $2\theta = 33°$. It is attributed to belite, a dicalcium silicate common in anhydrous cement. The formation of belite can be explained by a recombination phenomenon between the silicon from clayey phases and the calcium from dolomite (Xie et al., 2016). However, the low crystallinity of this new phase does not allow us to determine the type of polymorph. At 900°C all the peaks of dehydrated Ca-smectite and biotite disappeared, reflecting a complete loss of crystallinity of these two phases. This loss of crystallinity is correlated with recrystallization phenomena since the formation of new crystalline phases is observed. Among them we find akermanite ($Ca_2MgSi_2O_7$), augite ($(Si,Al)_2O_6)(Ca,Mg,Fe,Ti,Al)_2$ and enstatite ($Mg_2Si_2O_6$). Quartz and hydroxylapatite ($Ca_5(PO_4)_3OH$) are not affected by the heat treatment since no relevant change is observed between the raw sample and the 900°C calcined samples. Thus, the argillaceous-carbonate material turned out to be sensitive to the heat treatment since loss of crystallinity of the clay phases, decomposition of dolomite and recrystallization of new phases have been observed.

Figure 5 compares SEM images of raw (Figure 5A) and the 800°C calcined (Figure 5B) sample powders. Calcination at 800°C does not change the morphology of the material. Indeed, the shape of the mineral particle is almost identical before and after calcination. Yet the XRD analysis shows that at 800°C the dolomite has transformed into Lime and Periclase and that palygorskite has lost its crystallinity. It therefore appears that the morphology of the material does not reflect changes in chemistry and structure induced by calcination. A deeper investigation of the changes in the structure of the clay phases as a function of the calcination temperature was performed by ^{27}Al and ^{29}Si MAS NMR.

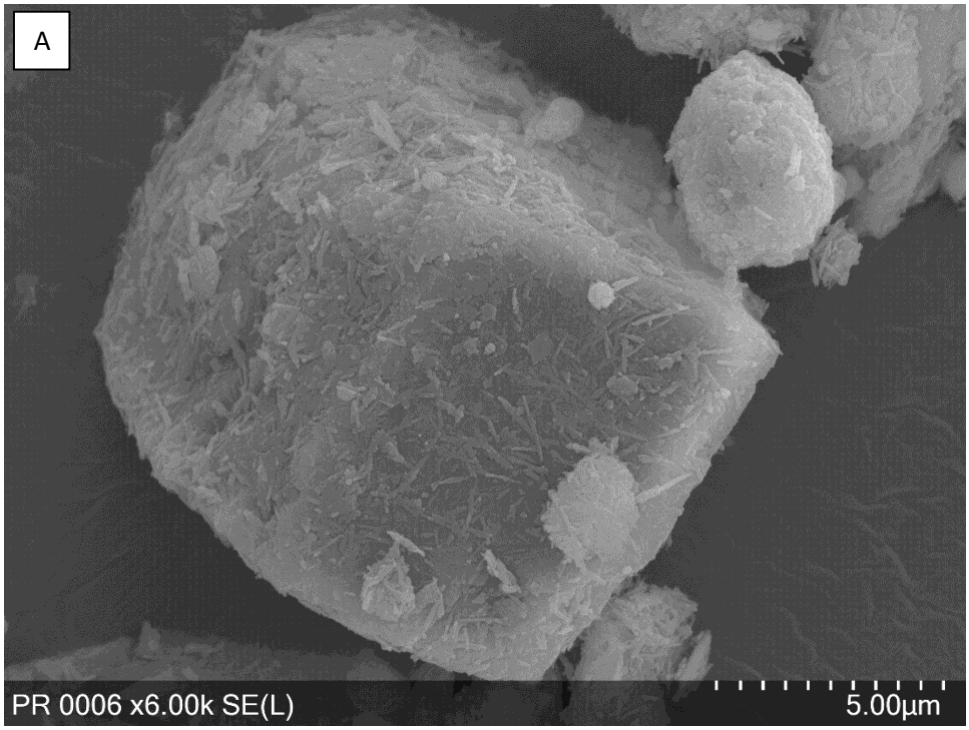

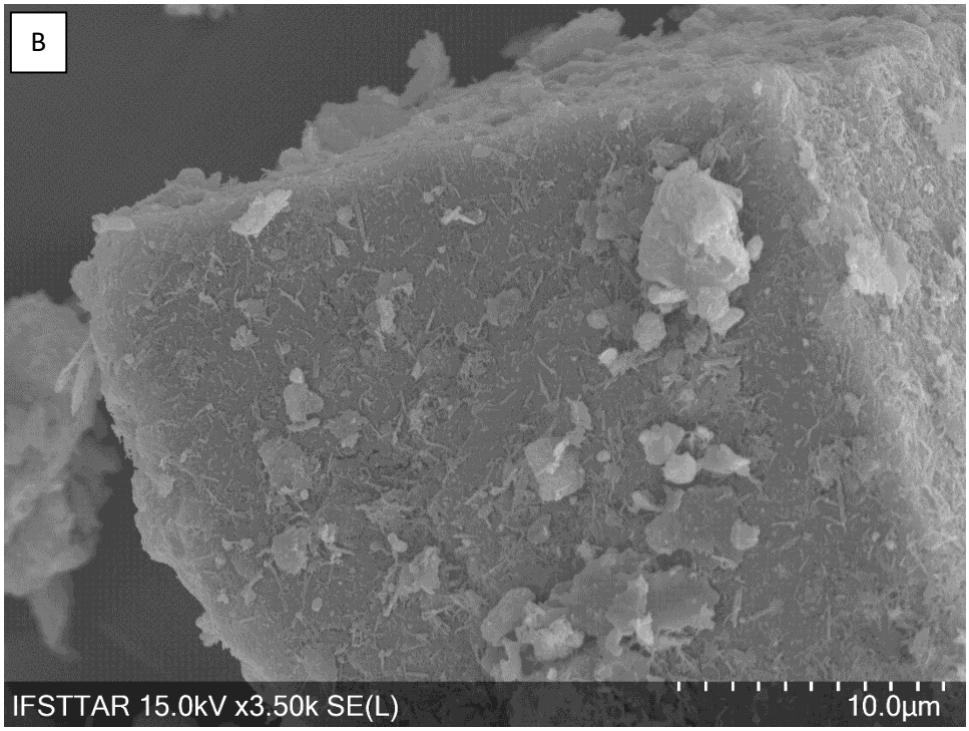

Figure 5: Scanning Electron Microscope images of the argillaceous-carbonate powder before (A) and after calcination at 800°C (B).

Aluminium NMR, through the observation of the change in coordination of aluminium atoms, allows us to characterize the dehydroxylation phenomenon of phyllosilicates induced by calcination.

Figure 3 displays the evolution of the ^{27}Al MAS NMR spectra of the argillaceous-carbonate samples as a function of the calcination temperature. The temperature increase leads to a diminution of the intensity of the resonance associated with hexacoordinated aluminium (3 ppm) and the appearance of two new resonances at around 59 and 27 ppm. These two new resonances can be associated with tetra and pentacoordinated aluminium, respectively (Maia et al., 2014). The decrease in the proportion of 6-fold aluminium and the formation of 4 and 5-fold aluminium is a consequence of the dehydroxylation resulting from the calcination of the sample. The temperature increase leads to the release of hydroxyl groups linked to the clay octahedra, resulting in a decrease of the coordination number of the aluminium atoms.

Figure 6 gives the relative proportions of the 6-, 5- and 4-fold aluminium atoms having been quantified by spectral integration of the ^{27}Al NMR spectra (details in Supporting Information). At 600°C a significant dehydroxylation of the argillaceous phases is observed since Al (VI) evolves from 87% to 36%. By using the Rietveld quantification of the crystal phases and their ideal theoretical chemical compositions we can calculate the contribution of each phase to the total amount of aluminium in the sample: 62% of the total aluminium comes from Ca-smectite, 34% from palygorskite and 4% from biotite. It becomes clear that this decrease of more than half in the proportion of Al (VI) cannot be due to the dehydroxylation of palygorskite only. So it seems that Ca-smectite start to dehydroxylate at 600°C, without fully losing its crystallinity since its signal remains detectable by XRD up to 800°C. These results are in agreement with the observations made by Fernandez et al. (2011) who suggested that the small amount of hydroxyl groups present in the smectite structure could explain the small effect of dehydroxylation on its cristallinity. On the other hand, as observed in Figure 1, there is a disappearance of the characteristic peaks of palygorskite from 600°C onwards. This strongest thermal reactivity of palygorskite compared to Ca-smectite could be explained by its particular TOT structure.

The hatched part of the total 6-fold aluminium in Figure 6 corresponds to the component (see Supporting Information) close to the signature of the aluminium present in palygorskite and smectite octahedra. It can be explained by octahedral sheets that resisted calcination. On the other hand, the dotted part corresponds to the component associated with very distorted octahedra. It can be seen that their relative proportions do not vary in the same way with increasing temperature, specifically, the proportion of 6-fold aluminium belonging to distorted sheets decreases less rapidly with increasing temperature. It can be hypothesized that the passage of 6-fold to 5-fold aluminium is made through this intermediate state corresponding to distorted octahedral sheets.

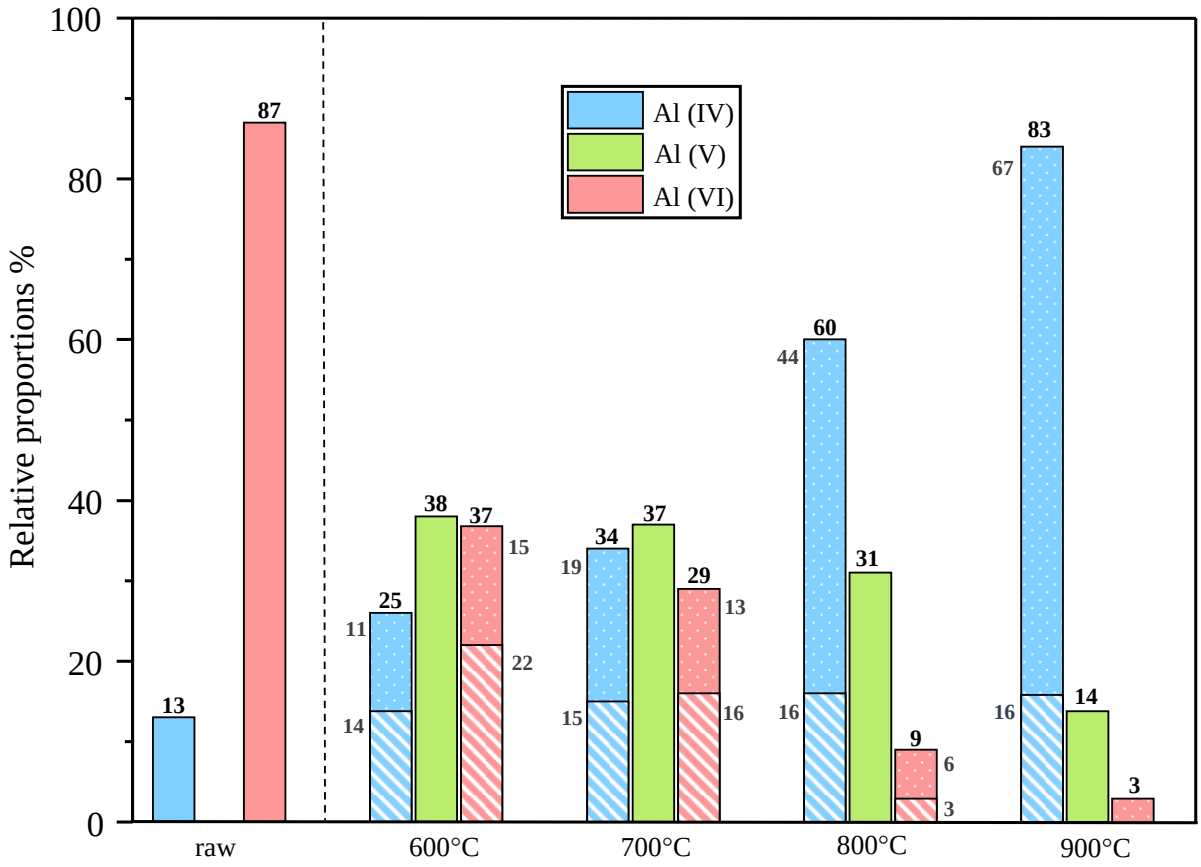

Figure 6: Relative proportions of the 6-, 5- and 4-fold aluminium atoms as a function of the calcination temperature.

From 600°C onwards 4-fold aluminium is formed (from 13 to 26 %). As for 6-fold aluminium, the 4-fold aluminium resonance is described by two components represented by hatched and dotted parts in Figure 6. The isotropic chemical shift of the "hatched" component of the 4-fold aluminium is 69 ppm (see supporting information) and could be associated with 4-fold aluminium in q3 configuration (Pardal et al., 2012). In contrast, the much lower isotropic chemical shift of the "dotted" component at 61 ppm can be associated with 4-fold aluminium in q4 configuration (Muller et al., 1986).

The "hatched" component appears as soon as the calcination temperature reaches 600°C and remains stable (around 15%) in spite of the temperature increase. Knowing that palygorskite becomes amorphous at 600°C (see Figure 1), we can associate this "hatched" component of 4-

fold aluminium with the dehydroxylation of palygorskite. Thereafter, only the "dotted" component of 4-fold aluminium increases with the increase of the calcination temperature, it would seem that this 4-fold aluminium is associated with the dehydroxylation of Ca-smectite and biotite.

Concerning the 5-fold aluminium, the highest proportion is reached from 600°C, and then decreases with increasing temperature. Up to 800°C its proportion remains stable because the dehydroxylation of 6-fold aluminium compensates for the transformation of 5-fold aluminium into 4-fold aluminium. Fernandez et al. (2011) associated the pozzolanic activity of a calcined clay with the appearance of penta-coordinated aluminum within the structure of the clay. Indeed, penta-coordinated aluminum turns out to be the most unstable form and the most prone to react. However, it is important to remember that 4-fold aluminium is also reactive and could play an important role in the pozzolanic reaction.

Therefore, 800°C seems to be a good calcination temperature since it allows an almost total dehydroxylation of the clay phases (only 9% of 6-fold aluminium remains) while keeping a large proportion of 5-fold aluminium (31%).

Table 2 displays the result of the Rietveld refinement of the 800°C calcined argillaceous-carbonate. An amorphous phase is present and accounts for almost 28% of the total sample mass. This high proportion of amorphous is mainly due to the amorphisation of palygorskite as its signal is no longer observable at 800°C (Figure 1). The formation of hematite at 800°C shows that part of the dolomite ($CaMg(CO_3)_2$) is actually ankerite ($Ca(Fe,Mg)(CO_3)_2$). However, the proportion of ankerite is very low in regards to the proportion of hematite formed (1.45 wt.%), which confirms the low iron value in chemical analysis results (Table 1).

Figure 4 displays the evolution of the ^{29}Si MAS NMR spectra of the argillaceous-carbonate sample as function of the calcination temperature. From 600°C, we can observe a broadening

of the resonances characteristic of the Q3 of the clayey phases. This broadening of the lines reflects distribution of the silicon atoms environments and so indicates the increase in disorder within the clay phases. The characteristic resonances of palygorskite are now almost indistinguishable, which confirms the observations made by XRD and suggests that the disappearance of its XRD peaks is not only due to its loss of crystallinity but also to strong distortions within its structure.

At 700°C the broadening of the Q3 resonances continues, which shows that the loss of crystallinity of the clayey phases continues. The main information is the appearance of a new resonance at -71 ppm which is not common in the MAS NMR analysis of a calcined clay. Skibsted (Skibsted et al., 1995) associates it with the presence of monomeric Q0 orthosilicates typical of belite (C_2S) one of the anhydrous phases of the clinker. That confirms the observations made by XRD and the possible reaction between silicon from clayey phases and calcium from dolomite. The trend will continue at 800°C with a widening of the Q3 resonances and an increase in the proportion of Q0 associated with belite. There is also the appearance of a new resonance at -74 ppm which can be associated with silicon in Q1 configuration (Janes and Oldfield, 1985) which is attributed to akermanite detected by XRD. By crossing these results with XRD, we can highlight that recrystallization phenomena begin as early as 800°C, but the low crystallinity of these new phases prevents their characterization by XRD at this temperature.

Between 800 and 900°C the width of Q0 resonance of belite decreases whereas its intensity increases. This means that the proportion and the level of crystallinity of the neo-formed belite are increasing. The Q1 resonance of akermanite is also more intense. The characteristic Q2 resonances of the augite (-72 ppm) and the enstatite (-84 ppm) cannot be observed because they overlap with the broader resonances from the calcined clay (MacKenzie and Meinhold, 1994; Huang et al., 2012).

It is important to specify that the chosen repetition time does not allow to be quantitative for quartz. Indeed, after several tests it seems that it is necessary to use a T_1 close to 3600 seconds to allow a complete relaxation, which complicates quantification. We have then calculated the proportion of belite formed at 800°C from the results of chemical analysis (XRF), quantification of crystal phases (XRD) and ^{29}Si MAS NMR. In order to carry out this calculation we made the hypothesis that Quartz does not react. Knowing the total amount of silicon (from XRF results) and the wt.% proportion of quartz (from XRD Rietveld refinement) in the raw sample we re-calculated the total amount of silicon present in the system without quartz. Then, by using the ^{29}Si MAS NMR spectrum of calcined sample, we quantified the relative repartition of silicon belonging to the belite and to the rest of the system (without quartz) at 800°C and we calculated their respective molar proportions. Subsequently, neglecting the minor phases, we used theoretical ideal formulas for palygorskite, smectite, and belite to convert molar proportions of silicon to weight proportions of phases. Calculations give a proportion of ~8 wt.% of belite in the sample calcined at 800°C. If we compare this value with the amount of crystalline belite obtained by Rietveld refining (~4,5 wt.%), it appears that the low crystallinity of belite causes the XRD to underestimate it by half.

The formation of belite during the calcination of a mixture of palygorskite and dolomite has already been observed (Xie et al., 2016). belite represents on average 15 to 20% of the total cement phases and is responsible of the long-term mechanical properties (Bouzidi et al., 2014). Its presence in the sample calcined at 800°C is therefore good news, assuming that it is reactive. However, the formation of lime and periclase could be troublesome for further use in cement systems (carbonation and post-hardening swelling).

5. CONCLUSION

The study of the thermal reactivity of this argillaceous carbonate highlighted its potential for a use as a SCM. Indeed, the palygorskite which composes this sample seems to be very sensitive to heat treatment and it dehydroxylated very easily from 600°C, certainly because of its so particular structure. Moreover, the calcination of the clay mixed with carbonate allowed to highlight the formation of belite (C_2S) from 700°C. The chemistry of the system favours the reaction of calcium from dolomite and silicon from clayey phases to form this cementitious phase. The calcined palygorskite associated with belite formation make this carbonate-material a very interesting system for use as a cementitious addition because of its double reactivity (pozzolanic and hydraulic). For the rest, it would be interesting to study the influence of the clay phase/carbonate ratio on the quality and quantity of neoformed belite and finally to test the reactivity of this sample.

ACKNOWLEGDMENTS

Dr. Bruno Lanson and Nathaniel Findling are thanked for their valuable help with the use of Profex software for Rietveld refinement.

References

Bala, P., Samantaray, B.K., Srivastava, S.K., 2000. Dehydration transformation in Ca-montmorillonite. Bull. Mater. Sci. 23, 61–67. https://doi.org/10.1007/BF02708614

Barron, P.F., Frost, R.L., Qlil, N., 1985. Solid state 29Si NMR examination of the 2:1 ribbon magnesium silicates, sepiolite and palygorskite. Am. Mineral. 70, 758–766.

Blanco, C., González, F., Pesquera, C., Benito, I., Mendioroz, S., Pajares, J.A., 1989. Differences Between One Aluminic Palygorskite and Another Magnesic by Infrared Spectroscopy. Spectrosc. Lett. 22, 659–673. https://doi.org/10.1080/00387018908053926

Bonavetti, V.L., Rahhal, V.F., Irassar, E.F., 2001. Studies on the carboaluminate formation in limestone filler-blended cements. Cem. Concr. Res. 31, 853–859. https://doi.org/10.1016/S0008-8846(01)00491-4

Boudriche, L., Calvet, R., Hamdi, B., Balard, H., 2011. Effect of acid treatment on surface properties evolution of attapulgite clay: An application of inverse gas chromatography. Colloids Surf. Physicochem. Eng. Asp. 392, 45–54. https://doi.org/10.1016/j.colsurfa.2011.09.031

Bouzidi, M.A., Tahakourt, A., Bouzidi, N., Merabet, D., 2014. Synthesis and Characterization of belite Cement with High Hydraulic Reactivity and Low Environmental Impact. Arab. J. Sci. Eng. 39, 8659–8668. https://doi.org/10.1007/s13369-014-1471-2

Brown, I.W.M., MacKenzie, K.J.D., Meinhold, R.H., 1987. The thermal reactions of montmorillonite studied by high-resolution solid-state 29Si and 27Al NMR 3265–3275.

Cancio Díaz, Y., Sánchez Berriel, S., Heierli, U., Favier, A.R., Sánchez Machado, I.R., Scrivener, K.L., Martirena Hernández, J.F., Habert, G., 2017. Limestone calcined clay cement as a low-carbon solution to meet expanding cement demand in emerging economies. Dev. Eng. 2, 82–91. https://doi.org/10.1016/j.deveng.2017.06.001

Danner, T., Norden, G., Justnes, H., 2018a. Characterisation of calcined raw clays suitable as supplementary cementitious materials. Appl. Clay Sci. 162, 391–402. https://doi.org/10.1016/j.clay.2018.06.030

Danner, T., Norden, G., Justnes, H., 2018b. Characterisation of calcined raw clays suitable as supplementary cementitious materials. Appl. Clay Sci. 162, 391–402. https://doi.org/10.1016/j.clay.2018.06.030

Doebelin, N., Kleeberg, R., 2015. *Profex* : a graphical user interface for the Rietveld refinement program *BGMN*. J. Appl. Crystallogr. 48, 1573–1580. https://doi.org/10.1107/S1600576715014685

El-Diadamony, H., Amer, A.A., Sokkary, T.M., El-Hoseny, S., 2018. Hydration and characteristics of metakaolin pozzolanic cement pastes. HBRC J. 14, 150–158. https://doi.org/10.1016/j.hbrcj.2015.05.005

Escalante, J.I., Gómez, L.Y., Johal, K.K., Mendoza, G., Mancha, H., Méndez, J., 2001. Reactivity of blast-furnace slag in Portland cement blends hydrated under different conditions. Cem. Concr. Res. 31, 1403–1409. https://doi.org/10.1016/S0008-8846(01)00587-7

Fernandez, R., Martirena, F., Scrivener, K.L., 2011. The origin of the pozzolanic activity of calcined clay minerals: A comparison between kaolinite, illite and montmorillonite. Cem. Concr. Res. 41, 113–122. https://doi.org/10.1016/j.cemconres.2010.09.013

Frydman, L., Harwood, J.S., 1995. Isotropic Spectra of Half-Integer Quadrupolar Spins from Bidimensional Magic-Angle Spinning NMR 5367–5368.

Galan, E., 1996. Properties and applications of palygorskite-sepiolite clays. Clay Miner. 31, 443–453. https://doi.org/10.1180/claymin.1996.031.4.01

Garg, N., Skibsted, J., 2016. Pozzolanic reactivity of a calcined interstratified illite/smectite (70/30) clay. Cem. Concr. Res. 79, 101–111. https://doi.org/10.1016/j.cemconres.2015.08.006

Garg, N., Skibsted, J., 2014. Thermal Activation of a Pure Montmorillonite Clay and Its Reactivity in Cementitious Systems. J. Phys. Chem. C 118, 11464–11477. https://doi.org/10.1021/jp502529d

Hollanders, S., Adriaens, R., Skibsted, J., Cizer, Ö., Elsen, J., 2016. Pozzolanic reactivity of pure calcined clays. Appl. Clay Sci. 132–133, 552–560. https://doi.org/10.1016/j.clay.2016.08.003

Horpibulsuk, S., Phojan, W., Suddeepong, A., Chinkulkijniwat, A., Liu, M.D., 2012. Strength development in blended cement admixed saline clay. Appl. Clay Sci. 55, 44–52. https://doi.org/10.1016/j.clay.2011.10.003

Huang, X., Ni, W., Cui, W., Wang, Z., Zhu, L., 2012. Preparation of autoclaved aerated concrete using copper tailings and blast furnace slag. Constr. Build. Mater. 27, 1–5. https://doi.org/10.1016/j.conbuildmat.2011.08.034

Huntzinger, D.N., Eatmon, T.D., 2009. A life-cycle assessment of Portland cement manufacturing: comparing the traditional process with alternative technologies. J. Clean. Prod. 17, 668–675. https://doi.org/10.1016/j.jclepro.2008.04.007

Ipavec, A., Gabrovšek, R., Vuk, T., Kaučič, V., Maček, J., Meden, A., 2011. Carboaluminate Phases Formation During the Hydration of Calcite-Containing Portland Cement: Carboaluminate Phase Formation. J. Am. Ceram. Soc. 94, 1238–1242. https://doi.org/10.1111/j.1551-2916.2010.04201.x

Janes, N., Oldfield, E., 1985. Prediction of silicon-29 nuclear magnetic resonance chemical shifts using a group electronegativity approach: applications to silicate and aluminosilicate structures. J. Am. Chem. Soc. 107, 6769–6775. https://doi.org/10.1021/ja00310a004

Krishnan, S., Emmanuel, A.C., Shah, V., Parashar, A., Mishra, G., Maity, S., Bishnoi, S., 2019. Industrial production of limestone calcined clay cement: experience and insights. Green Mater. 7, 15–27. https://doi.org/10.1680/jgrma.18.00003

Lippmaa, E., Maegi, M., Samoson, A., Engelhardt, G., Grimmer, A.R., 1980. Structural studies of silicates by solid-state high-resolution silicon-29 NMR. J. Am. Chem. Soc. 102, 4889–4893. https://doi.org/10.1021/ja00535a008

Mackenzie, K.J.D., Brown, I.W.M., Cardile, C.M., Meinhold, R.H., 1987. The thermal reactions of muscovite studied by high-resolution solid-state 29-Si and 27-Al NMR. J. Mater. Sci. 22, 2645–2654. https://doi.org/10.1007/BF01082158

MacKenzie, K.J.D., Meinhold, R.H., 1994. The thermal reactions of talc studied by 29Si and 25Mg MAS NMR. Thermochim. Acta 244, 195–203. https://doi.org/10.1016/0040-6031(94)80219-X

Maia, A.Á.B., Angélica, R.S., de Freitas Neves, R., Pöllmann, H., Straub, C., Saalwächter, K., 2014. Use of 29Si and 27Al MAS NMR to study thermal activation of kaolinites from Brazilian Amazon kaolin wastes. Appl. Clay Sci. 87, 189–196. https://doi.org/10.1016/j.clay.2013.10.028

Massiot, D., Fayon, F., Capron, M., King, I., Le Calvé, S., Alonso, B., Durand, J.-O., Bujoli, B., Gan, Z., Hoatson, G., 2002. Modelling one- and two-dimensional solid-state NMR spectra: Modelling 1D and 2D solid-state NMR spectra. Magn. Reson. Chem. 40, 70–76. https://doi.org/10.1002/mrc.984

Morodome, S., Kawamura, K., 2009. Swelling Behavior of Na- and Ca-Montmorillonite up to 150°C by in situ X-ray Diffraction Experiments. Clays Clay Miner. 57, 150–160. https://doi.org/10.1346/CCMN.2009.0570202

Muller, D., Gessner, W., Samoson, A., Lippmaa, E., 1986. Solid-state Aluminium-27 Nuclear Magnetic Resonance Chemical Shift and Quadrupole Coupling Data for Condensed AIO4, Tetrahedra. J Chem Soc Dalton Trans 5.

Olszak-Humienik, M., Jablonski, M., 2015. Thermal behavior of natural dolomite. J. Therm. Anal. Calorim. 119, 2239–2248. https://doi.org/10.1007/s10973-014-4301-6

Pardal, X., Brunet, F., Charpentier, T., Pochard, I., Nonat, A., 2012. 27Al and 29Si Solid-State NMR Characterization of Calcium-Aluminosilicate-Hydrate. Inorg. Chem. 51, 1827–1836. https://doi.org/10.1021/ic202124x

Prasad, M.S., Reid, K.J., Murray, H.H., 1991. Kaolin: processing, properties and applications. Appl. Clay Sci. 6, 87–119. https://doi.org/10.1016/0169-1317(91)90001-P

Sakai, E., Miyahara, S., Ohsawa, S., Lee, S.-H., Daimon, M., 2005. Hydration of fly ash cement. Cem. Concr. Res. 35, 1135–1140. https://doi.org/10.1016/j.cemconres.2004.09.008

Sanz, J., Serratosa, J.M., 1984. Silicon-29 and aluminum-27 high-resolution MAS-NMR spectra of phyllosilicates. J. Am. Chem. Soc. 106, 4790–4793. https://doi.org/10.1021/ja00329a024

Scrivener, K., Martirena, F., Bishnoi, S., Maity, S., 2018. Calcined clay limestone cements (LC3). Cem. Concr. Res. 114, 49–56. https://doi.org/10.1016/j.cemconres.2017.08.017

Skibsted, J., Jakobsen, H.J., Hall, C., 1995. Quantification of calcium silicate phases in Portland cements by 29Si MAS NMR spectroscopy. J. Chem. Soc. Faraday Trans. 91, 4423. https://doi.org/10.1039/ft9959104423

Soltani, A., Tarighat, A., Varmazyari, M., 2018. Calcined Marl and Condensed Silica Fume as Partial Replacement for Ordinary Portland Cement. Int. J. Civ. Eng. 16, 1549–1559. https://doi.org/10.1007/s40999-018-0289-9

Trümer, A., Ludwig, H.-M., Schellhorn, M., Diedel, R., 2019. Effect of a calcined Westerwald bentonite as supplementary cementitious material on the long-term performance of concrete. Appl. Clay Sci. 168, 36–42. https://doi.org/10.1016/j.clay.2018.10.015

W.F.Bradley, 1940. The structural scheme of attapulgite, in: American Mineralogist. pp. 405–410.

Xie, J., Chen, T., Xing, B., Liu, H., Xie, Q., Li, H., Wu, Y., 2016. The thermochemical activity of dolomite occurred in dolomite–palygorskite. Appl. Clay Sci. 119, 42–48. https://doi.org/10.1016/j.clay.2015.07.014

SUPPORTING INFORMATIONS

Spectral decompositions of the ^{27}Al MAS spectra were done by using the dmfit software (Massiot et al., 2002). The initial fit was constructed from the spectrum of the argillaceous-carbonate calcined at 600°C. The relevance of this fit is supported by ^{27}Al 3QMAS (Frydman and Harwood, 1995) spectrum of the same sample. Signal from 6-fold aluminium that resisted calcination are represented by a Lorentzian line (labelled L6_hatched). In order to account for the asymmetry of the ^{27}Al resonances (due to the presence of Electric Field Gradient distributions) in this amorphous sample, we chose the 'Czsimple' shape implemented in dmfit with d=5 to use the Gaussian Isotropic Model. The isotropic chemical shift distribution is described by an independent Gaussian distribution. Thus, a 'Czsimple' line (labelled C6_dotted) was used to complete the description of the 6-fold aluminium resonance. A single 'Czsimple' line (labelled C5) was used for the 5-fold aluminium resonance. Finally, two 'Czsimple' lines (labelled C4_hatched and C4_dotted) were mandatory to fully describe the 4-fold aluminium resonance. Parameters for the five lines are gathered in Table 3. Except amplitudes, all other parameters were kept constant when fitting the ^{27}Al MAS spectra of the argillaceous-carbonate samples calcined at 700, 800 and 900°C. Table 4 gives the relative proportions of the lines as a function of the calcination temperature.

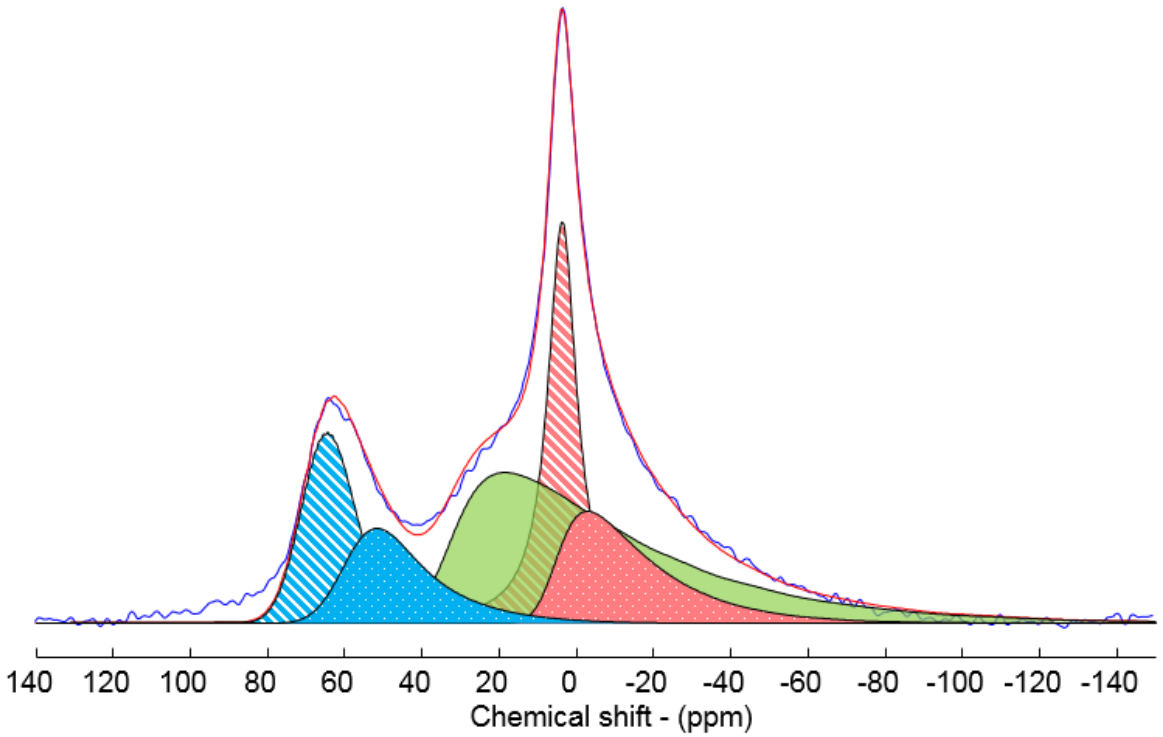

559

560 **Figure S1: Spectral integration of the ^{27}Al MAS NMR spectrum of the argillaceous-carbonate**

561 **calcined at 600°C**

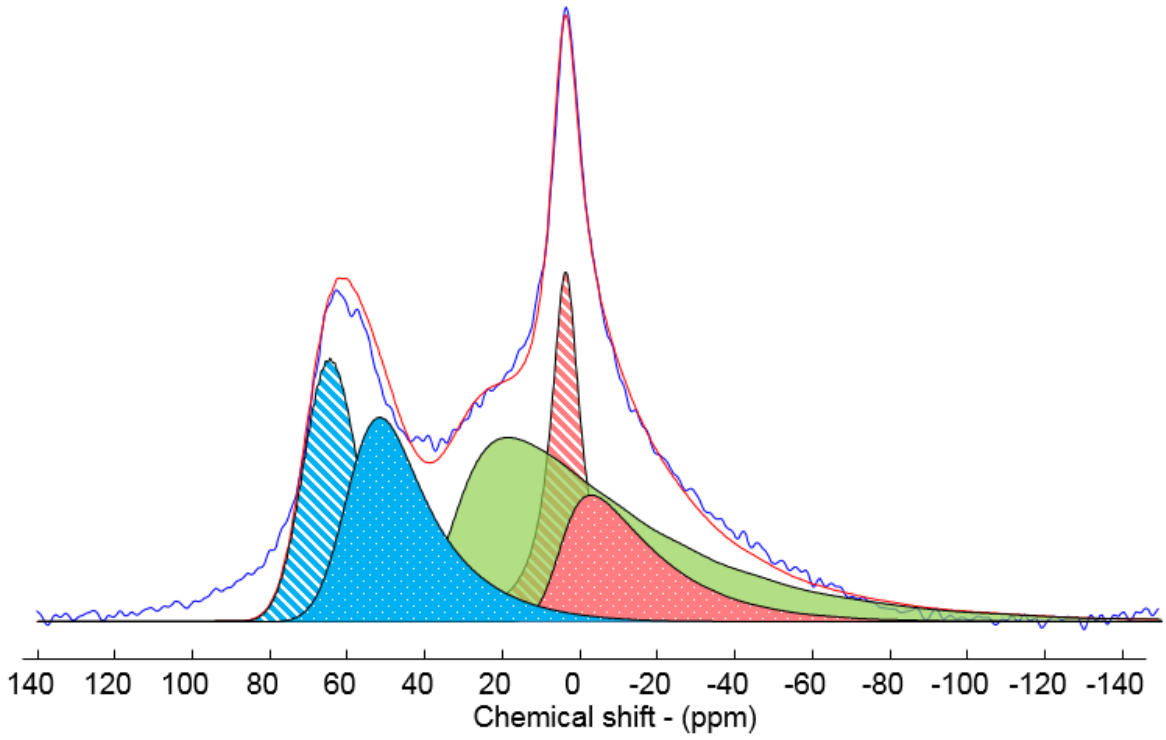

562

Figure S2: Spectral integration of the ^{27}Al MAS NMR spectrum of the argillaceous-carbonate calcined at 700°C

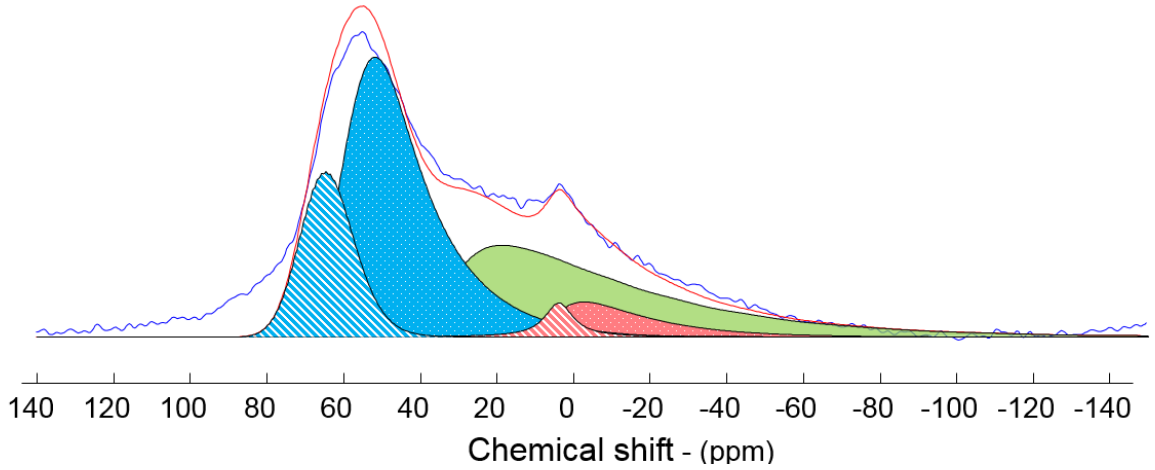

Figure S3: Spectral integration of the ^{27}Al MAS NMR spectrum of the argillaceous-carbonate calcined at 800°C

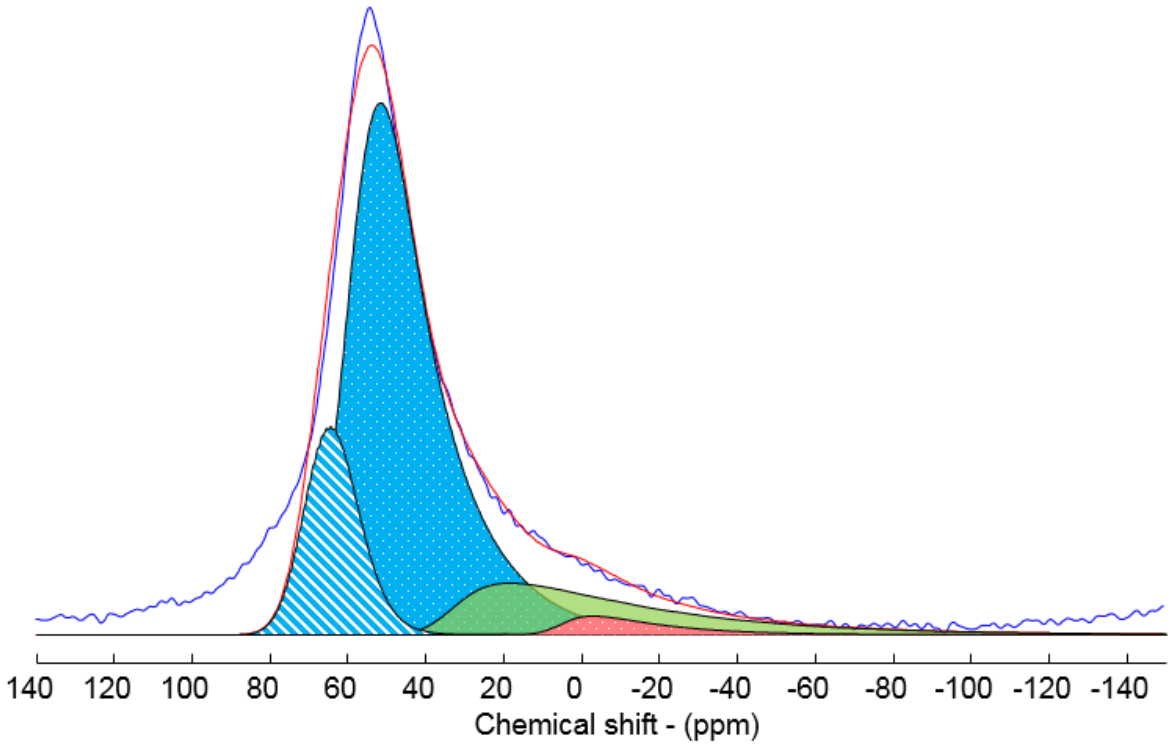

Figure S4: Spectral integration of the ^{27}Al MAS NMR spectrum of the argillaceous-carbonate calcined at 900°C

Table S1: Parameters for the ^{27}Al MAS NMR spectral decompositions. δiso is the isotropic chemical shift, C_Q is the mean quadrupolar product (GIM) and FWHM CS is the full width at half maximum of the Gaussian distribution of isotropic chemical shift.

Component	Shape	δ_{iso} (ppm)	Width (ppm)	C_Q (MHz)	FWHM CS (ppm)
L6_hatched	Lorentzienne	3.8	9.0		
C6_dotted	CzSimple	6.5		7.0	10.0
C5	CzSimple	35.0		10.0	14.0
C4_dotted	CzSimple	61.0		6.5	15.0
C4_hatched	CzSimple	69.0		3.5	14.0

Table S2: Relative Proportions of the components of ^{27}Al MAS NMR spectra as function of the calcination temperature

	C4_hatched	C4_dotted	C5	L6_hatched	C6_dotted
600°C	14	11	38	22	15
700°C	15	19	37	16	13
800°C	16	44	31	3	6
900°C	16	67	14	0	3

The Rietveld quantification of the raw and calcined material at 800°C was performed using the Profex Rietveld refinement program (Doebelin and Kleeberg, 2015). Ideal structural phases

have been used and refined as best as possible. The sample is a natural sample made of a mixture of several phases, which explains the difficulty in obtaining a perfect fit. For the raw sample two different palygorskite crystal structures (palygorskite1 and palygorskite2) and two dolomite (dolomite and dolomite2) have been necessary to optimize the fit. The high R_{wp} value for the refinement of the raw sample is explained by a difficulty to fit the shape of the characteristic peaks of dolomite. The presence of a low proportion of ankerite may explain this difficulty. Concerning the refinement of the 800°C calcined material, to simulate the dehydrated smectite, crystalline structure of a zero-water layer potassium smectite was used.

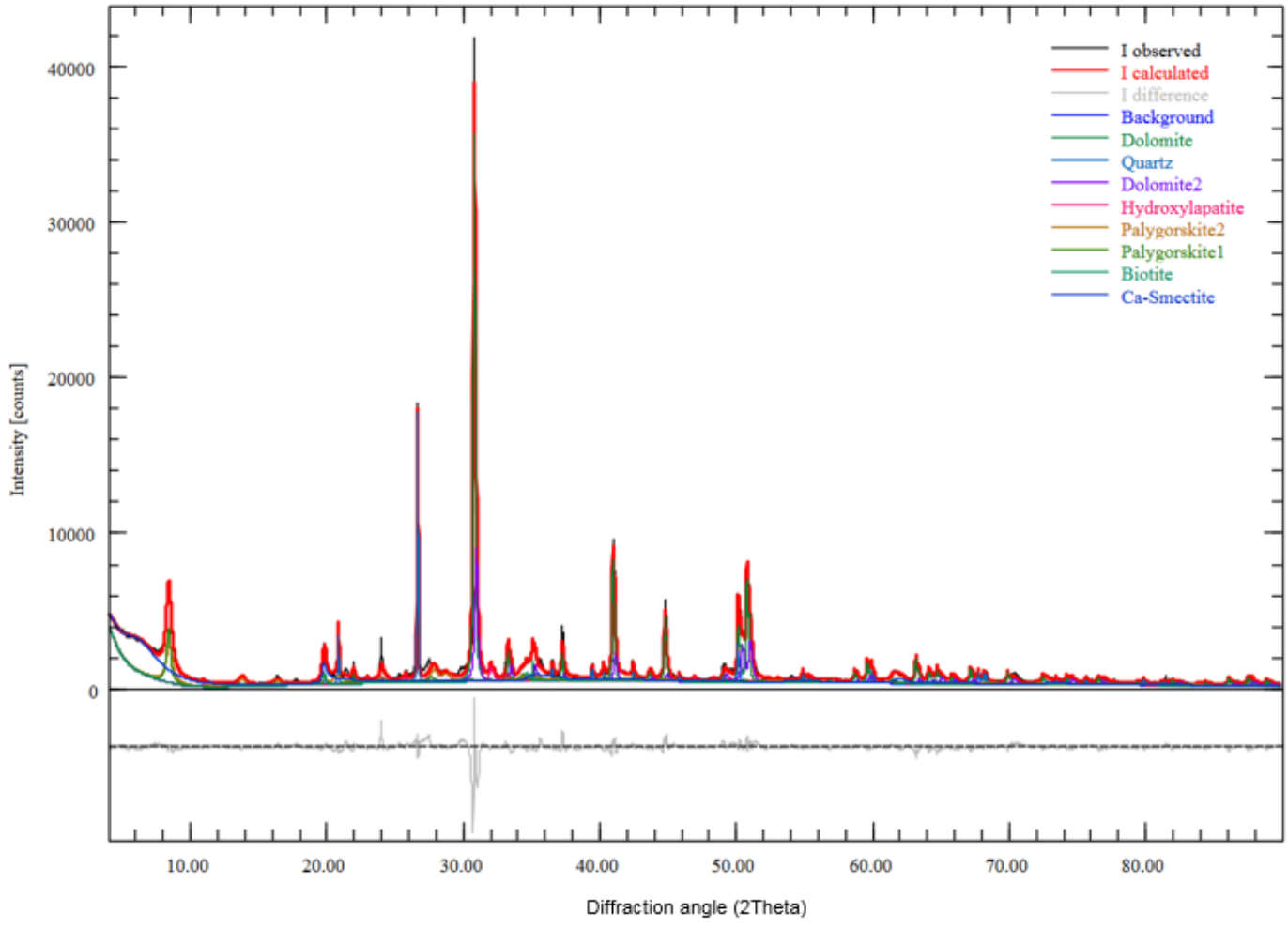

Figure S5 : Rietveld refinement of the raw argillaceous-carbonate (with peaks of phases)

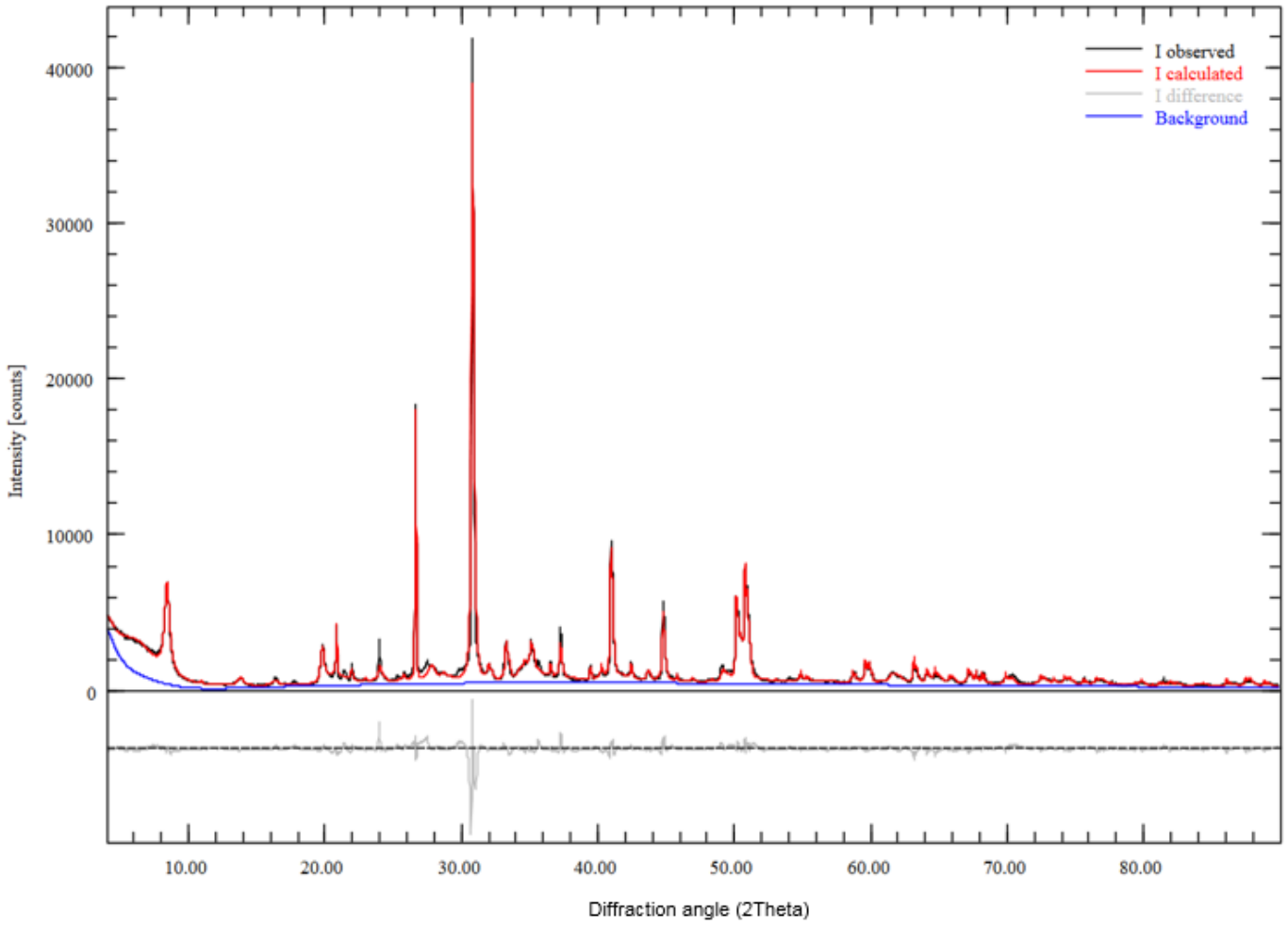

Figure S6 : Rietveld refinement of the raw argillaceous-carbonate (without peaks of phases)

Table S3: Statistics of the Rietveld refinement of the raw argillaceous-carbonate

Statistics	R_{wp} = 10.24	R_{exp} = 3.14	X^2 = 10.63	GoF = 3.26

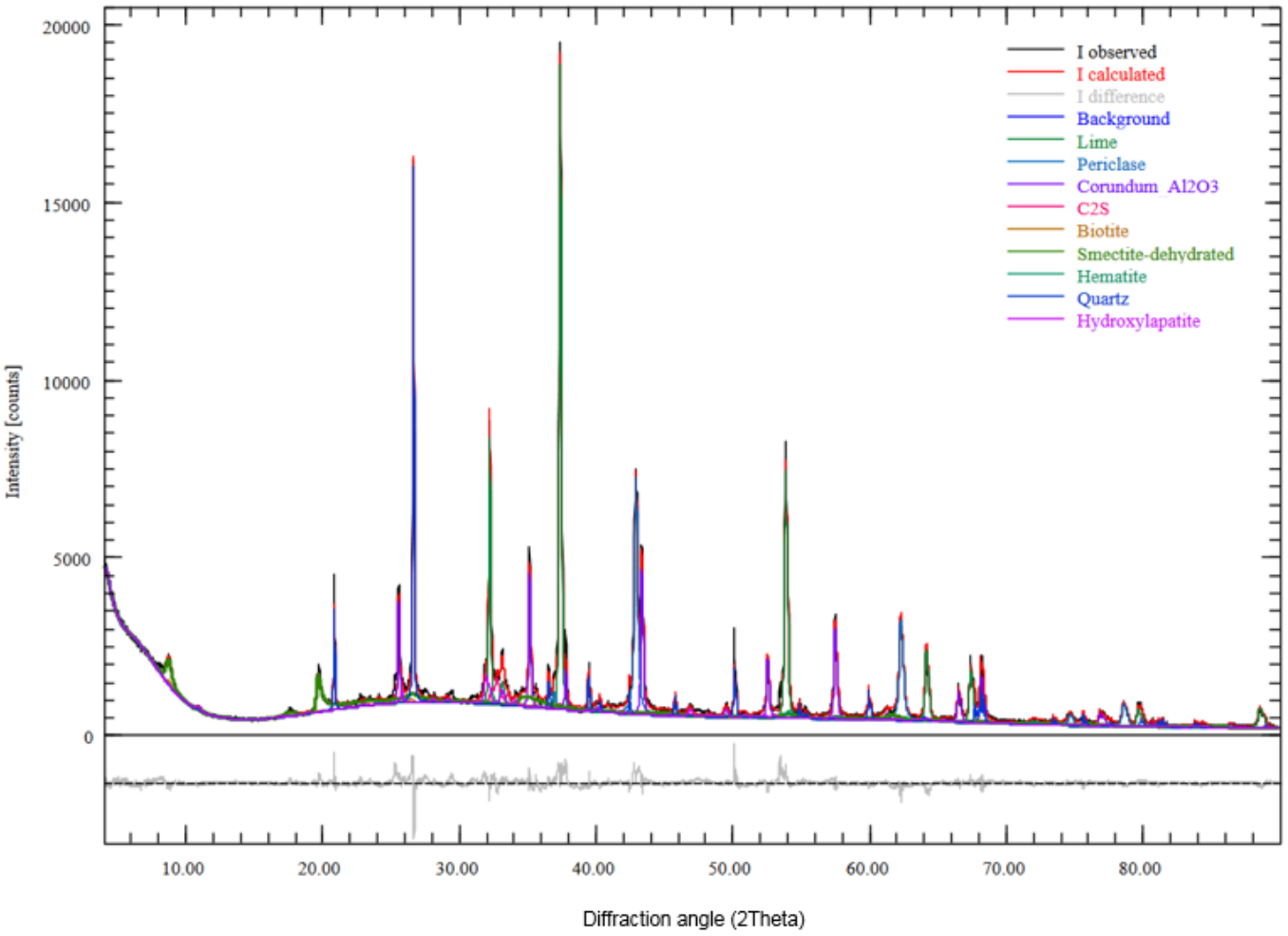

Figure S7 : Rietveld refinement of the argillaceous-carbonate calcined at 800°C (with peaks of phases)

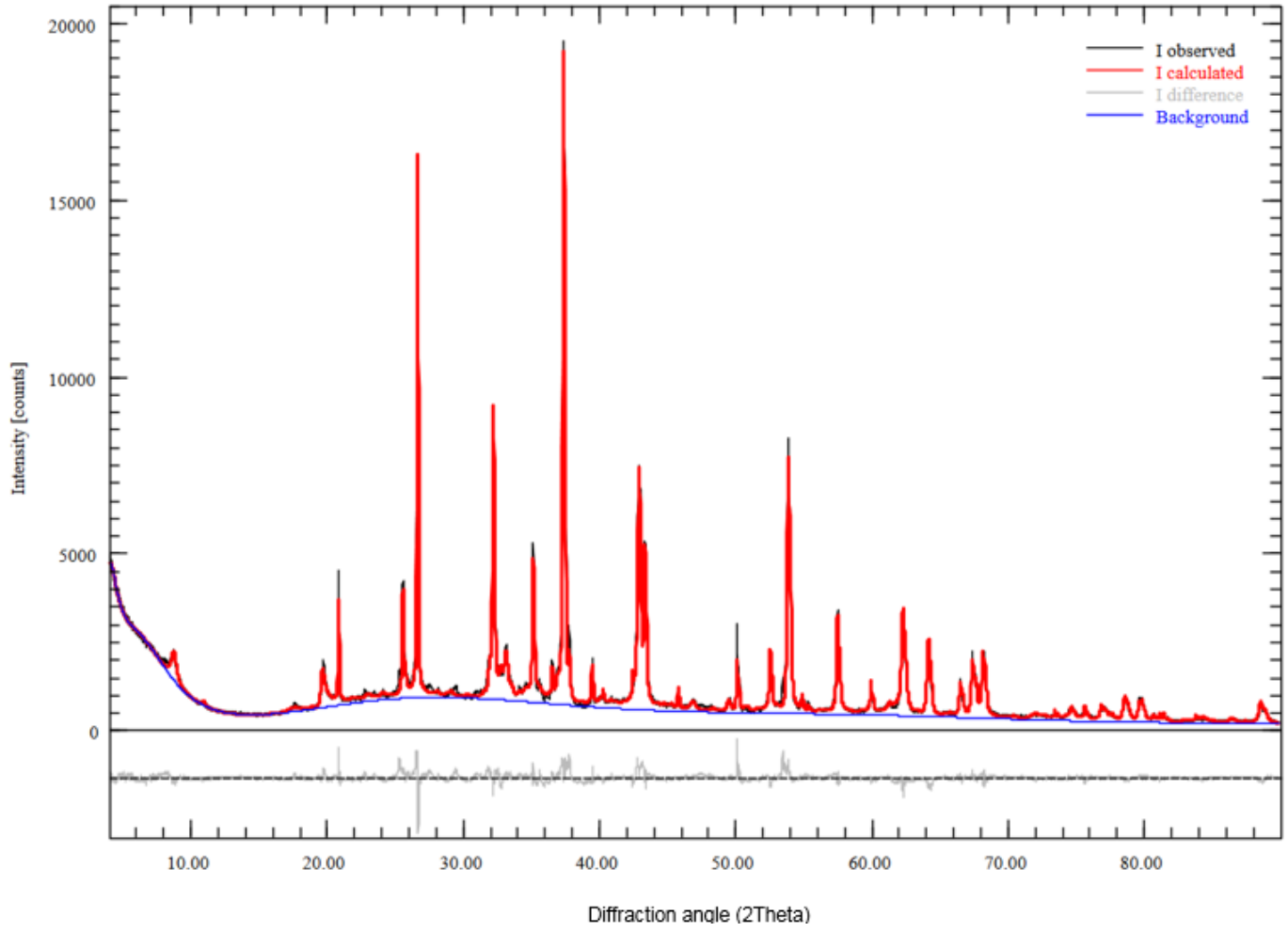

Figure S8 : Rietveld refinement of the argillaceous-carbonate calcined at 800°C (without peaks of phases)

Table S4: Statistics of the Rietveld refinement of the argillaceous-carbonate calcined at 800°C

Statistics	R_{wp} = 6.74	R_{exp} = 3.26	X^2 = 4.27	GoF = 2.07

References

Doebelin, N., Kleeberg, R., 2015. *Profex* : a graphical user interface for the Rietveld refinement program *BGMN*. J. Appl. Crystallogr. 48, 1573–1580. https://doi.org/10.1107/S1600576715014685

Frydman, L., Harwood, J.S., 1995. Isotropic Spectra of Half-Integer Quadrupolar Spins from Bidimensional Magic-Angle Spinning NMR 5367–5368.

Massiot, D., Fayon, F., Capron, M., King, I., Le Calvé, S., Alonso, B., Durand, J.-O., Bujoli, B., Gan, Z., Hoatson, G., 2002. Modelling one- and two-dimensional solid-state NMR spectra: Modelling 1D and 2D solid-state NMR spectra. Magn. Reson. Chem. 40, 70–76. https://doi.org/10.1002/mrc.984